2

Wireless Telemetry for Implantable Biomedical Microsystems

Farzad Asgarian and Amir M. Sodagar
Integrated Circuits & Systems (ICAS) Lab.,
Department of Electrical & Computer Eng.,
K. N. Toosi University of Technology,
Iran

1. Introduction

Rapid development of microelectronics during the past years allowed the emergence of high-performance *implantable biomedical microsystems* (IBMs). Nowadays, these systems share many features and basic components, and are being used in different applications such as neural signal recording, functional muscular stimulation, and neural prostheses. Due to implant size limitations in a wide range of applications, and the necessity for avoiding wires to reduce the risk of infection, wireless operation of IBMs is inevitable. Hence, an IBM is usually interfaced with an external host through a wireless link. In order to minimize the complexity and size of an implant, most of the signal processing units are kept outside the body and embedded in the external host. Moreover, the power needed for the implant modules including a central processing and control unit, stimulators and sensors is transmitted by the external host via wireless interfacing. The wireless link is also used for bidirectional data transfer between the implanted device and the outside world. Thus, as shown in Fig. 1, the wireless interface on the implant needs to contain a power regulator, a demodulator for receiving control/programming data (*forward data telemetry*), and a modulator for sending the recorded signals and implant status to the external host (*reverse data telemetry*).

Daily increase in the complexity of IBMs leads to demand for sending higher power and data rates towards the implants. This is more obvious in high-density stimulating microsystems such as visual prostheses. Therefore, forward telemetry, which is the main focus of this chapter, has an important role in today's high-performance IBMs.

Design of RF links for power and data telemetry is usually performed based on both system-level aspects (i.e., functional architecture and physical structure), and power transfer efficiency and data rate requirements. This includes physical design of the link, carrier frequency and power of the RF signal, data rate, and also modulation scheme considered for forward and reverse data telemetry. It should be added that there are other important concerns that need to be studied in this area, such as safety levels for the exposure of the human body to electromagnetic waves.

This chapter begins with a discussion on limitations in the design of wireless links due to electromagnetic safety standards. Then, different types of wireless links are introduced and compared, following which, the trend towards multiple carrier links is highlighted. In

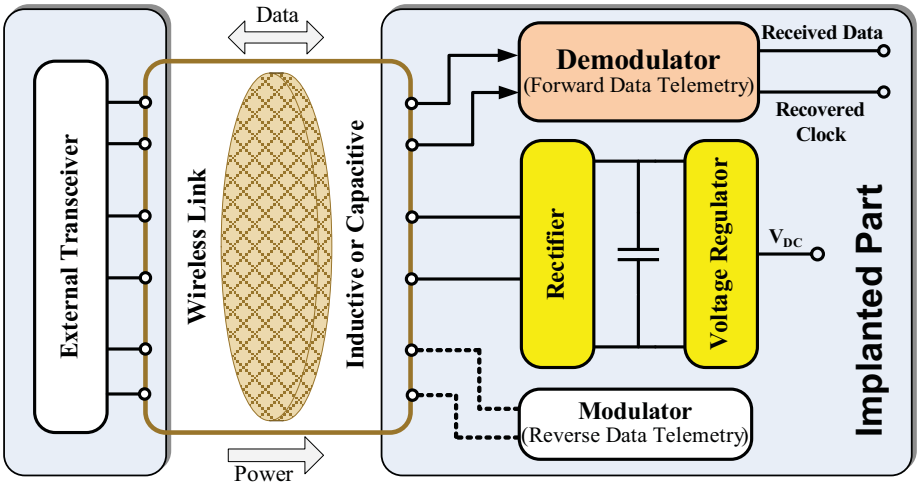

Fig. 1. General block diagram of the wireless interface.

forward data telemetry, commonly-used modulation schemes along with their pros and cons are studied. Finally, recent works on clock recovery and demodulator circuits are presented in detail.

2. Biological concerns

2.1 IEEE standard C95.1-2005

Electromagnetic fields generated by telemetry systems can potentially lead to power dissipation in living tissues and consequently cause damages to the tissue that are sometimes irreversible. Hence, when designing a device capable of wireless data exchange with the external world, it is an inseparable part of the designer's responsibility to make sure that the RF energy generated by the device fulfills the safety levels enforced by the standards for the exposure of human body to RF energy. This is a major concern in the design of wireless portable devices such as laptops and cell phones, and IBMs are not exceptions. Designer of a wireless link needs to make sure that potentially hazardous fields are not exceeded, as indicated in some electromagnetic safety standards. One of the well-known resources in this area is the IEEE standard for safety levels with respect to human exposure to radio frequency electromagnetic fields, 3 KHz to 300 GHz (IEEE Std C95.1-2005). This standard emphasizes that *radio frequency* (RF) exposure causes adverse health effects only when the exposure results in detrimental increase in the temperature of the core body or localized area of the body. For frequencies between 100 KHz and 3 GHz (which are used in most telemetry applications), *basic restrictions* (BRs) are expressed in terms of *specific absorption rate* (SAR) in the standard. This is, indeed, the power absorbed by (dissipated in) unit mass of tissue (Lazzi, 2005). At any point of the human body, SAR is related to the electric field as

$$SAR(x,y,z) = \frac{\sigma(x,y,z)\,E^2(x,y,z)}{2\rho(x,y,z)} \tag{1}$$

where σ is the tissue conductivity (in S/m), ρ is the tissue density (Kg/m^3), and E is the electric field strength (V/m) at point *(x,y,z)*. Consequently, the SI unit of SAR is Watt per kilogram (W/Kg). In Table 1, BRs for whole-body and localized exposure for both the people in *controlled environments* and the *general public* when an RF safety program is unavailable (*action level*), are shown. The localized exposure BRs are expressed in terms of *peak spatial-average SAR* which is the maximum local SAR averaged over any 10-grams of tissue in the shape of a cube.

			SAR (W/Kg)	
			General public	**Persons in controlled environments**
Whole-body exposure		Whole-Body Average (WBA)	0.08	0.4
Localized exposure	**Localized**	Peak spatial average	2	10
	Extremities* & pinnae		4	20
* The extremities are the arms and legs distal from the elbows and knees, respectively.				

Table 1. BRs for frequencies between 100 KHz and 3 GHz (IEEE standard C95.1-2005).

It should be noted that due to the difficulty in calculation of SAR values and for convenience in exposure assessment, *maximum permissible exposures* (MPEs), which are sometimes called *investigation levels*, are provided in this IEEE standard (Table. 2). However, two issues must be kept in mind. First, compliance with this standard includes a determination that the SAR limits are not exceeded. This means that if an exposure is below the BRs, the MPEs can be exceeded. Second, in some exposure conditions, especially when the body is extremely close to an RF field source and in highly localized exposures (which is the case in IBMs), compliance with the MPEs may not ensure that the local SARs comply with the BRs. Therefore, for IBMs, SAR evaluation is necessary and the MPEs cannot be used.

Frequency range (MHz)	**RMS electric field strength (V/m)**	**RMS magnetic field strength (A/m)**
0.1-1.34	614	$16.3/f_M$
1.34-3	$823.8/f_M$ *	$16.3/f_M$
3-30	$823.8/f_M$	$16.3/f_M$
30-100	27.5	$158.3/f_M^{1.668}$
100-400	27.5	0.0729
* f_M is the frequency in MHz.		

Table 2. MPE for general public (IEEE standard C95.1-2005).

2.2 SAR calculation

In order to estimate the electric field and SAR in the human body, numerical methods of calculation can be used. One of the most commonly used numerical techniques for electromagnetic field dosimetry, is the *finite-difference time-domain* (FDTD) method, which is a direct solution of Maxwell's curl equations in the time domain. Most of electromagnetic simulators (e.g., SEMCAD X by SPEAG and CST Microwave Studio), in conjunction with computational human-body models, can perform FDTD and SAR calculations. In recent

years, *three-dimensional* (3-D) whole body human models have been developed based on high-resolution *magnetic resonance imaging* (MRI) scans of healthy volunteers (Dymbylow, 2005; Christ et al., 2010). Providing a high level of anatomical details, these models play an important role in optimizing evaluation of electromagnetic exposures, e.g. in the human body models presented in (Christ et al., 2010) more than 80 different tissue types are distinguished.

3. Wireless links

3.1 Inductive links

The wireless link for forward power and data telemetry is mostly implemented by two closely-spaced, inductively coupled coils (Fig. 2). The secondary coil is implanted in the human body and the primary coil is kept outside. Usually these coils are a few millimeters apart, with thin layers of living tissues in between. In this approach, normally both sides of the link are tuned to the same resonant frequency to increase the power transmission efficiency (Sawan et al., 2005; Jow & Ghovanloo, 2009). This frequency is known as the carrier frequency and is limited to a few tens of megahertz for transferring relatively large amounts of energy to the implant. This is due to the fact that power dissipation in the tissue, which results in excessive temperature rise, increases as the carrier frequency squared (Lin, 1986). Employing low-frequency carriers is also supported by recent SAR calculations, e.g. in the telemetry link of an epiretinal prosthesis reported in (Singh et al., 2009), the SAR limit of the IEEE standard would be crossed around 16 MHz for a normalized peak current of 0.62 A in the primary coil. Thus, for power transmission, carrier frequencies of inductive links are typically chosen below 15 MHz (Jow & Ghovanloo, 2007 & 2009; Simard et al., 2010).

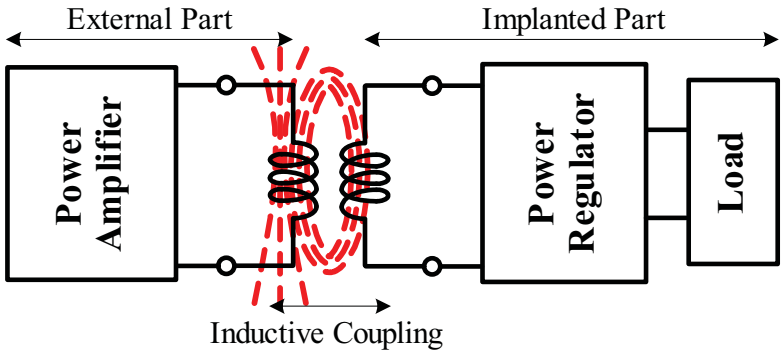

Fig. 2. General block diagram of an inductive power link

In order to convert the dc voltage of an external DC power supply (or battery) to a magnetic field, the primary coil is driven by a power amplifier, as illustrated in Fig. 3(a). In these biomedical applications, usually a class-E amplifier is used because of its high efficiency which is theoretically near 100% (Socal, 1975). As the coils are mutually coupled, magnetic field in the *primary coil* (L_1) induces an ac voltage on the *secondary coil* (L_2). This voltage is then rectified and regulated to generate the dc supply voltages required to operate the implanted electronics. To simplify the efficiency equations, usually the *mutual inductance* (M) of the coils is normalized with respect to L_1 and L_2 by defining K as the *coils coupling coefficient* (Jow and Ghovanloo; 2007)

$$K = \frac{M}{\sqrt{L_1 L_2}} . \tag{2}$$

Moreover, the rectifier, the regulator and the power consumption of all implanted circuits are modeled with an equivalent ac resistance R_L (Kendir et al., 2005; Van Schuglenbergh & Puers, 2009). A simplified schematic for an inductive link is shown in Fig. 3(a) for efficiency calculations. The resistor R_1 is a combination of *effective series resistance* (ESR) of L_1 (used to estimate coil losses) and the output resistance of the power amplifier, while R_2 is the ESR of L_2 (Liu et al., 2005; Harrison, 2007). The capacitors C_1 and C_2 are used to create a resonance on the primary and secondary sides of the link, respectively at

$$\omega_0 = \frac{1}{\sqrt{L_1 C_1}} = \frac{1}{\sqrt{L_2 C_2}} . \tag{3}$$

It is worth noting that C_2 is in fact a combination of the added capacitor and the parasitic capacitance of the secondary coil.

Efficiency of the secondary side of the link (η_2) can be calculated by transforming R_2 to its parallel equivalent at resonance, R_{P2} (Fig. 3(b))

$$R_{P2} = R_2 (1+Q_2^2) \approx Q_2^2 R_2 \tag{4}$$

where $Q_2=\omega_0 L_2/R_2$ is the *quality factor* of the unloaded-secondary circuit. In this case, R_L and R_{P2} both receive the same voltage and η_2 is given by

$$\eta_2 = \frac{R_{P2}}{R_{P2}+R_L} = \frac{Q_2}{Q_2+Q_L} \tag{5}$$

where $Q_L=\omega_0 R_L C_2=R_L/\omega_0 L_2$ is named as the *effective Q of the load network* (Baker & Sarpeshkar, 2007).

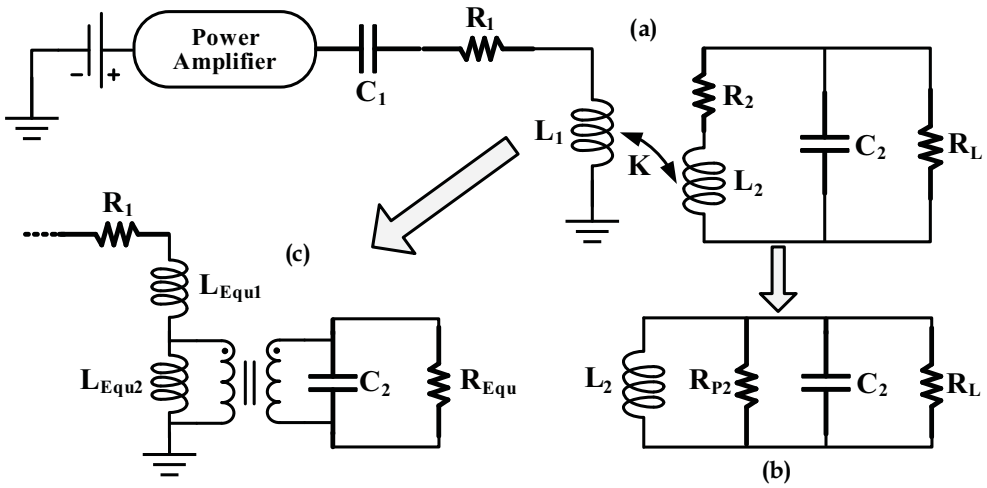

Fig. 3. (a) Simplified schematic of an inductive link. (b) and (c) Equivalent circuit diagrams.

To find the efficiency of the primary side of the link (η_1), first the coupling between the coils is modeled as an ideal transformer, and two inductances $L_{Equ1}=L_1(1-K^2)$ and $L_{Equ2}=K^2 L_1$ (Fig. 3(c)) (Harrison, 2007). Then, C_2 and $R_{Equ}=R_L \| R_{P2}$ are reflected through the ideal transformer, resulting in values of $C_{Reflect}=(C_2/K^2)(L_2/L_1)$ and $R_{Reflect}=(K^2L_1/K_2)\ R_{Equ}$. As $C_{Reflect}$ and L_{Equ2} resonate at ω_0, η_1 can be defined as

$$\eta_1 = \frac{R_{Reflect}}{R_{Reflect}+R_1} = \frac{K^2Q_1Q_2}{1+K^2Q_1Q_2+\frac{R_{P2}}{R_L}} = \frac{K^2Q_1Q_2}{1+K^2Q_1Q_2+\frac{Q_2}{Q_L}} \tag{6}$$

where $Q_1=\omega_0 L_1/R_1$ is the quality factor of the primary circuit in the absence of magnetic coupling. Therefore, total power efficiency for an inductive link is defined as:

$$\eta = \eta_1\eta_2 = \frac{K^2Q_1Q_2}{1+K^2Q_1Q_2+\frac{Q_2}{Q_L}} \times \frac{1}{1+\frac{Q_L}{Q_2}}. \tag{7}$$

Equation (7) shows that besides the loading network, η is affected by the coupling coefficient and the quality factors of the coils which are dependent on the coils' geometries, relative distance, and number of turns. For high efficiencies, both η_1 and η_2 should be maximized. This occurs when

$$1 << \frac{Q_2}{Q_L} = \frac{L_2}{R_L}\frac{1}{R_2C_2} << K^2Q_1Q_2 = \frac{K^2L_1}{L_2}\frac{1}{R_2C_2}. \tag{8}$$

However, in IBMs the coils are weakly coupled and K is typically below 0.4 (Kendir et al., 2005; Jow & Ghovanloo, 2009; Simard et al., 2010). Thus, depending on the application, the above conditions might not be satisfied and the overall link efficiency should be maximized with a different method. From equations (5) and (6), increasing Q_L decreases η_1 and increases η_2. This means that there is an optimum value for Q_L, for which the total efficiency is maximized (Baker & Sarpeshkar, 2007; Van Schuylenbergh &. Puers, 2009). In other words, one can determine an optimum loading condition that maximizes the total efficiency. By differentiating (7) with respect to Q_L, the optimum Q_L can be found as

$$Q_{L,opt} = \frac{Q_2}{\sqrt{1+K^2Q_1Q_2}}. \tag{9}$$

Consequently, maximum achievable efficiency is given by

$$\eta_{Max} = \frac{K^2Q_1Q_2}{(1+\sqrt{1+K^2Q_1Q_2})^2} \tag{10}$$

and is plotted as a function of $K^2Q_1Q_2$ in Fig. 4.

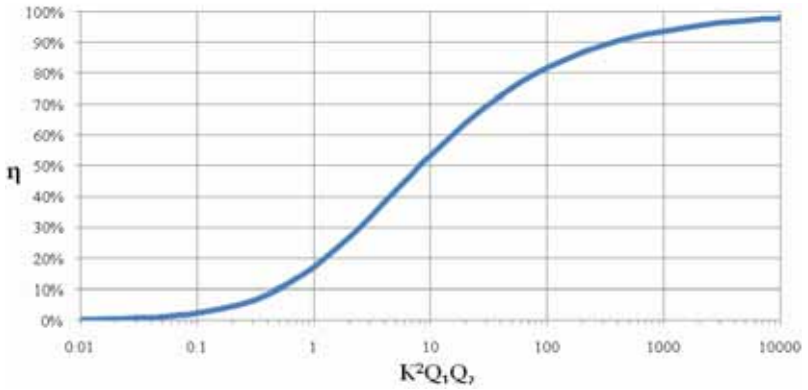

Fig. 4. Maximum achievable link efficiency as a function of $K^2Q_1Q_2$

Wire wound coils have been employed in IBM inductive links for many years. These coils are made of filament wires in the form of a single or multiple individually insulated strands twisted into circular shapes (Litz wires) which reduce the coil losses at high frequencies (Jow & Ghovanloo, 2007). To achieve higher efficiencies, mutual inductance between the primary and secondary coils can be increased by utilizing ferrite cores (Sodagar et al., 2009b). However, as illustrated in Fig. 5(a), with both air cores and ferromagnetic cores, the use of regular coils has a major drawback: Magnetic flux lines are formed around the primary coil as a result of the flow of current through it. They close their paths through the air and spread all around the coil. Therefore, the implanted sensitive analog circuitry is exposed to a major portion of the electromagnetic energy radiated by the primary coil. To reduce the electromagnetic interferences caused by inductive coupling, use of E-shape cores is proposed in (Sodagar et al., 2009b). As shown in Fig. 5(b), primary and secondary coils are wrapped across the cores' middle fingers. This method helps confine the electromagnetic flux within the ferrite cores by forming a closed magnetic circuit through which it can flow. The flux can only radiate some energy to the outside when it passes through the inevitable gap between the two coils. Fig. 5(c) shows a photograph of the coils used to power up a multichannel neural recording system utilizing this technique, which is presented in (Sodagar et al., 2009b). The E-shape ferrite coils are 5.4 mm × 2 mm × 2.7 mm (L×W×H) with the middle finger and the side fingers 1.5 mm and 0.7 mm thick, respectively.

Inductive links can also be implemented by employing *printed spiral coils* (PSCs). As wire-wound coils cannot be batch-fabricated or shrunk down in size without the use of sophisticated machinery (Jow & Ghovanloo, 2007), PSCs have drawn a lot of attention in recent years. Such planar coils are produced using standard photolithographic and micro fabrication techniques on flexible or rigid substrates. Thus, the geometrics of PSCs, which are important factors in the link power efficiency, can be accurately defined. A typical square-shaped PSC is shown in Fig. 6, in which D_o and D_i are the outer and inner diameters of the coil, W is the width of the tracks, and S is the track spacing. Because of size constraints, usually the outer diameter of implanted coils is limited to 10 mm, while the external coils might have larger diameters, depending on the application (Shah et al., 1998; Jow & Ghovanloo, 2007). Classically, in IBMs power and data are transferred through the same wireless link, with the data modulated on the same carrier used for power transfer. However, power transfer is more efficient with high-Q coils, while in many applications

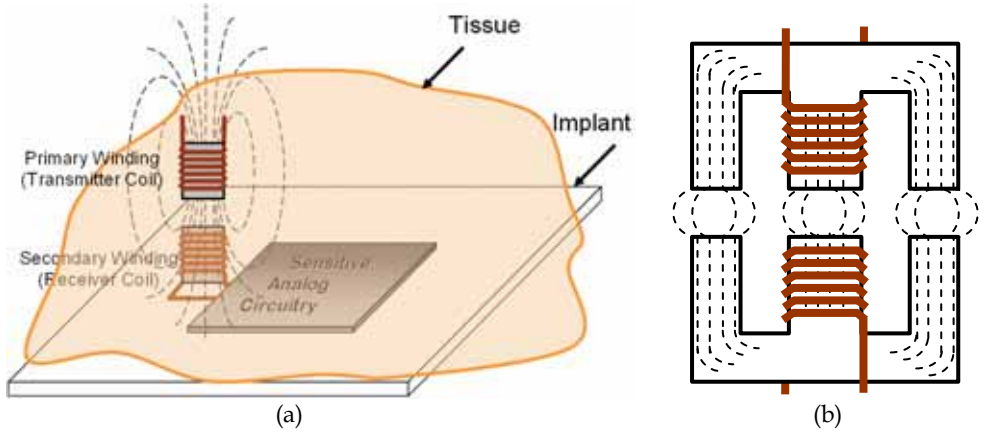

(a) (b)

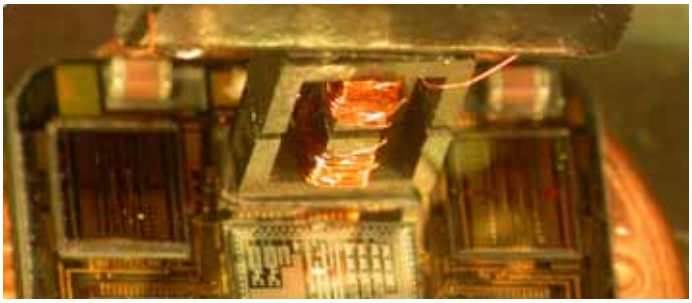

(c)

Fig. 5. (a) Problem of magnetic flux with regular coils. (b) Confining the magnetic flux by forming a closed magnetic circuit. (c) Implementation of the idea in (b) on the implantable device presented by (Sodagar et al., 2009b).

such as retinal implants, wideband data transfer is needed, demanding for low quality factors of the coils. Due to contradictory requirements of power and data transfer, there is a trend towards utilizing multiple carrier links in which separate coils are designed for power and data (Ghovanloo & Alturi, 2007; Jow & Ghovanloo, 2008; Simard et al., 2010). These links typically take advantage of PSCs for power transmission. As the data carrier amplitude is much smaller than the power carrier, crosstalk becomes an important issue in multiple carrier links design. Different geometries and orientations of data coils have been reported for solving this problem. In (Jow & Ghovanloo, 2008) vertical and figure-8 data coils are proposed to reduce the cross coupling between power and data coils. Vertical coils are wound across the diameter of the power PSCs, while figure-8 types are implemented as PSCs in the same substrate of the power PSCs and parallel to them. Results show that vertical coils attenuate the power carrier interference more, when the coils are perfectly aligned. On the other hand, figure-8 coils are less sensitive to horizontal misalignments. In (Simard et al., 2010) another geometry named coplanar geometry is presented. Based on the results, in comparison with vertical and figure-8 coils, this approach provides better immunity to crosstalk under misalignments. However, as the total area of the wireless link is increased, it might not be usable in some applications.

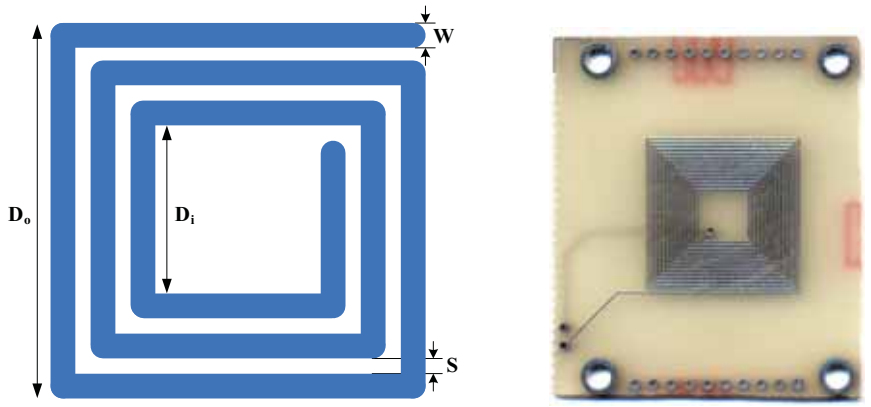

(a) (b)

Fig. 6. Typical squared-shaped PSCs. (a) Important geometrical parameters. (b). A prototype fabricated on a *printed circuit board (PCB)*.

Multiple carrier architectures allow designing and optimizing power and data links separately and based on their own specific requirements. As a result, optimized data links for different modulation techniques have been reported (Ghovanloo & Alturi, 2007; Simard et al., 2010). Furthermore, by increasing the quality factors of the power coils, efficiencies as high as 72% has been achieved (Jow & Ghovanloo, 2009).

3.2 Capacitive links

Although capacitive coupling has been already used for inter-chip data communication (Canegallo et al., 2007; Fazzi et al., 2008) and even for power transfer (Culurciello & Andreou, 2006), it was studied for implantable biomedical applications in (Sodagar & Amiri, 2009) for the first time. This method is based on capacitive coupling between two parallel plates. One of the plates is placed on the implant side and the other is attached to the skin on the external side. The plates are aligned to have maximum overlapping, while the skin and thin layers of tissue act as dielectric. In this approach, electric field is used as the carrier for power and data, contrary to the traditional inductive approach where magnetic field plays the key role. As illustrated in Fig. 7, the field lines defining the RF energy conveying power and data in capacitive links are well confined within the area considered for this purpose. This helps extremely reduce or even eliminate the relatively large electromagnetic interference on the sensitive analog circuitry in the system. A significant side benefit of this energy confinement is that several power, data and clock signals can be exchanged between the implant and the external setup without interfering with each other even at the same frequencies. Moreover, another important advantage of capacitive links is that they are naturally compatible with standard *integrated circuit* (IC) fabrication technologies.

A simplified schematic of a capacitive link is shown in Fig. 8, where V_{ext} is the input voltage, C_{Body1} and C_{Body2} are the capacitances between the implanted and external plates, C_{in} is the equivalent input capacitance of the circuits directly connected to the link, and R_L is the equivalent ac resistance of the loading network. The voltage received on the implant side, V_{int}, is determined as

$$V_{int} = V_{ext}\left[\frac{R_L^2(1+P)}{R_L^2(1+P)^2 + X_{Ceq}^2} + j\frac{R_L X_{Ceq}}{R_L^2(1+P)^2 + X_{Ceq}^2}\right] \tag{11}$$

where X_{Ceq} is the reactance of $C_{eq}=C_{Body1}+C_{Body2}$, and $P=C_{in}/C_{eq}$. Assuming $C_{in}<<C_{eq}$, equation (11) becomes

$$V_{int} = V_{ext}\left(\frac{R_L^2}{R_L^2 + X_{Ceq}^2} + j\frac{R_L X_{Ceq}}{R_L^2 + X_{Ceq}^2}\right), \tag{12}$$

and the voltage transfer rate is given by

$$\left|\frac{V_{int}}{V_{ext}}\right| = \sqrt{\frac{R_L^2}{R_L^2 + X_{Ceq}^2}}. \tag{13}$$

Thus, V_{int} is maximized when $X_{Ceq}<<R_L$.

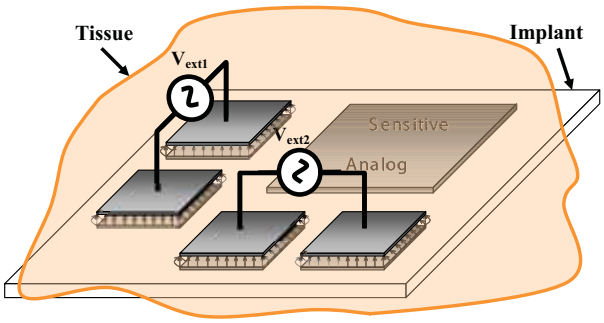

Fig. 7. Energy confinement in the capacitive coupling approach.

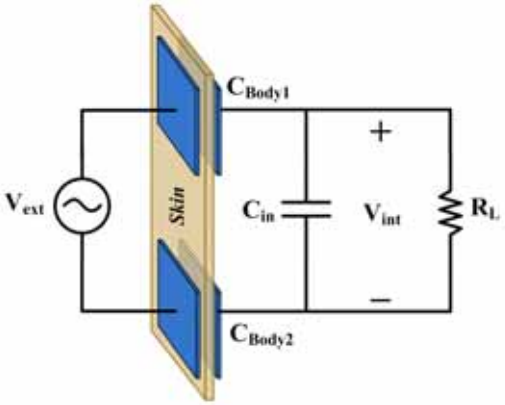

Fig. 8. Simplified schematic of a capacitive link.

Unit capacitances and reactance of 1 mm × 1 mm parallel plates 1 mm apart from each other are calculated and plotted in Figs. 9 and 10 for frequencies between 100 kHz and 10 MHz. Calculations are based on the dielectric properties of biological tissues at RF and microwave frequencies reported in (Gabriel et al., 1996a, b & c), which are also available as an internet resource by the *Italian National Research Council, Institute for Applied Physics* (IFAC). Fig. 9 shows that, in general, unit capacitances of the skin and muscle increase with the frequency. However, as illustrated in Fig. 10, unit reactance of dry skin decreases as the frequency increases, while unit reactances of wet skin and muscle are almost constant and only change about 20% over the frequency range 1 MHz – 10 MHz.

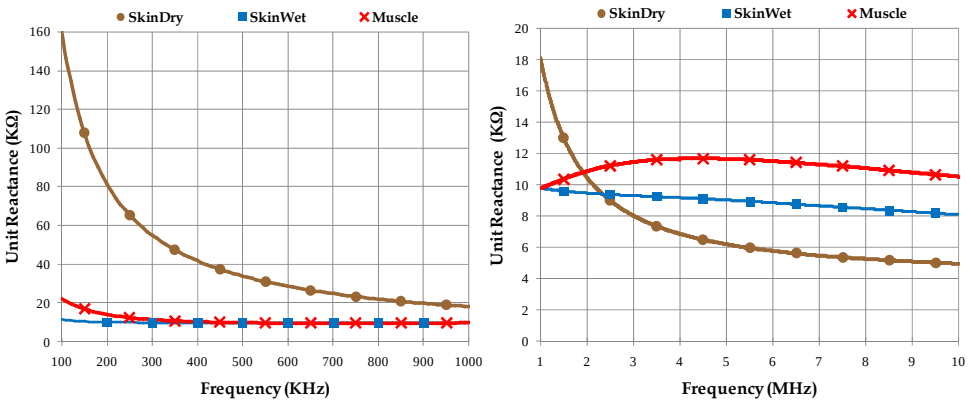

(a) (b)

Fig. 9. Unit capacitance of 1 mm × 1 mm plates 1 mm apart from each other for frequencies between (a) 100 kHz and 1 MHz, and (b) 1 MHz and 10 MHz

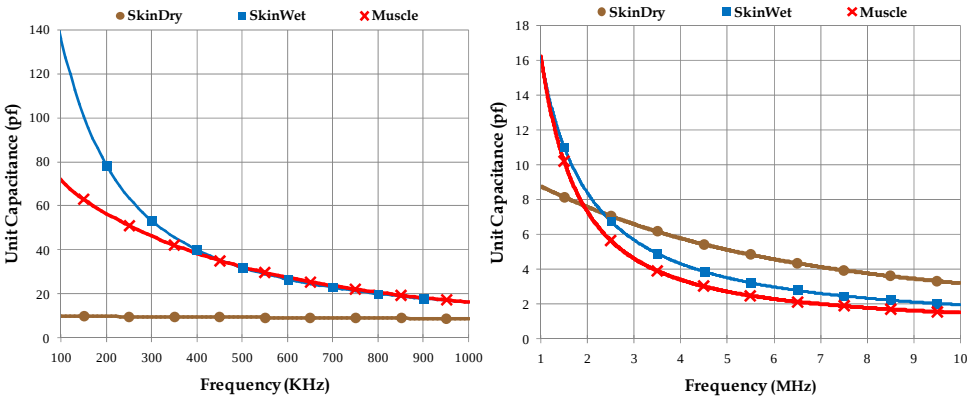

(a) (b)

Fig. 10. Unit reactance of 1 mm × 1 mm plates 1 mm apart from each other for frequencies between (a) 100 kHz and 1 MHz, and (b) 1 MHz and 10 MHz

According to Equation (13) R_L plays a key role in the voltage transfer rate of a capacitive link. Hence, it is of crucial importance to note that the value of R_L for power transfer through a telemetry link is completely different from the case where the link is used for data telemetry. Thus, similarly to inductive links, it is more practical to use the multiple carrier approach, and design each link separately. In data links, C_{Body1} and C_{Body2} are connected to high-impedance nodes, such as inputs of voltage buffers or comparators (Asgarian & Sodagar, 2010). This implies that even with small plates, voltage transfer rates close to 1 can be achieved. For instance, 2 mm × 2 mm plates 3 mm apart from each other result in a X_{Ceq} less than 4 kΩ (assuming dry skin as the dielectric), which is relatively much smaller than R_L in data links. On the other hand, in power transmission R_L is typically below 10 kΩ modeling substantial current draw from the power source. To optimize the voltage gain, X_{Ceq} should be kept as low as possible. This is achieved by choosing larger plates, while still complying with the implant size constraints. As an example, with dry skin as the dielectric and 5 mm × 5 mm plates 3 mm apart from each other, X_{Ceq} and voltage transfer rate are about 0.6 kΩ and 95%, respectively, for R_L=2 kΩ.

4. Data transfer to biomedical implants

4.1 Modulation schemes

Regardless of the type of the telemetry link, data needs to be modulated onto a carrier for wireless transmission. Forward data telemetry should be capable of providing a relatively high data rate, especially in applications where the implant interfaces with the central nervous system such as visual prostheses (Ghovanloo & Najafi, 2004). On the other hand, as discussed before, there are limitations on increasing the carrier frequency for implantable devices. Therefore, *data-rate-to-carrier-frequency (DRCF) ratio* is introduced as an important measure, indicating the amount of data successfully modulated on a certain carrier frequency. From among the different types of modulation schemes available for wireless data transfer, digital modulation techniques including *amplitude shift keying* (ASK), *frequency shift keying* (FSK), and *phase shift keying* (PSK) are more commonly used in IBMs. These modulations are illustrated in Fig. 11.

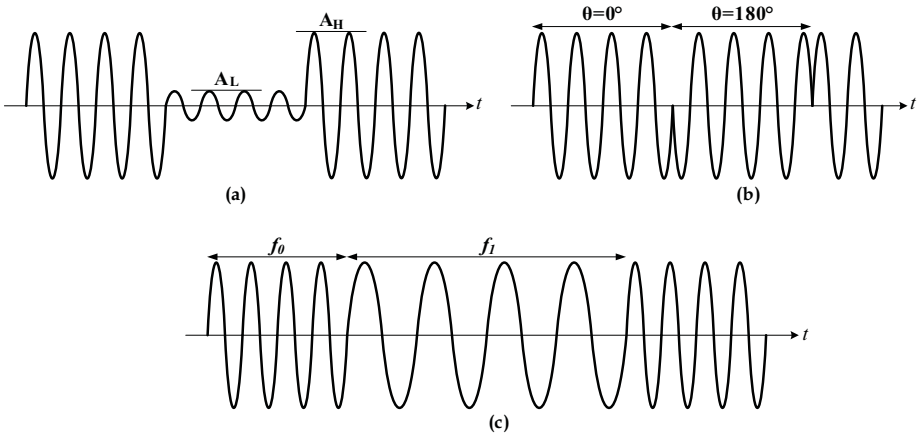

Fig. 11. Digital modulation schemes: (a) ASK, (b) PSK, and (c) FSK.

Although ASK has been used in some early works due to its simple modulation and demodulation circuitry, it suffers from low data rate transmission and high sensitivity to amplitude noise (Sodagar & Najafi, 2006; Razavi, 1998). In FSK, employing two different carrier frequencies limits the data rate to the lower frequency and consequently decreases the DRCF ratio. In contrast with FSK, PSK benefits from fixed carrier frequency and provide data rates as high as the carrier frequency (DRCF=100%).
In terms of *bit error rate* (BER), PSK exhibits considerable advantage over FSK and ASK at the same amplitude levels. This can be easily shown by plotting signal constellations or signal spaces for different modulation techniques (Fig. 12), and considering the fact that BER is mostly affected by the points with the minimum Cartesian distance in a constellation (Razavi, 1998). Additionally, a detailed analysis of two types of PSK modulation, *binary PSK* (BPSK) and *quadrature PSK* (QPSK) is given in (Razavi, 1998), which shows that they have nearly equal probabilities of error if the transmitted power, bit rate, and the differences between the bit energy and symbol energy are taken into account.

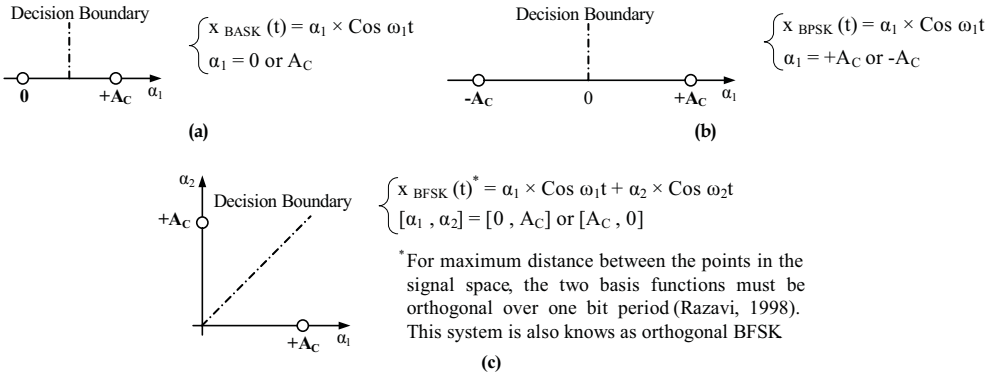

Fig. 12. Signal constellation of binary (a) ASK, (b) PSK, and (c) FSK modulations.

4.2 Data and clock recovery circuits

4.2.1 Amplitude Shift Keying (ASK)

One of the first techniques employed for digital data modulation in IBMs is ASK. In this technique, two carrier amplitude levels are assigned to logic levels "0" and "1", as illustrated in Fig. 11(a). Perhaps it was the straightforward implementation of both modulators and demodulators for ASK that attracted the interest of designers to this modulation scheme. To facilitate detection of ASK-modulated data on the receiver end and reduce the possibility of having errors in data transfer, there should be enough distinction between the two amplitude levels associated with 0's and 1's, A_L and A_H, respectively. *Modulation index (depth)* is a measure for this distinction, which is defined for ASK as:

$$m\% = \frac{A_H - A_L}{A_H} \times 100\% \tag{14}$$

It is, however, the nature of amplitude modulation techniques, e.g., AM for analog and ASK for digital, that makes them susceptible to noise. To overcome this weakness, modulation index is chosen as high as possible.

When used only for data telemetry (not for power telemetry), whether from the implant to the outside world or vice versa, ASK modulation index can be increased to even 100%. This extreme for ASK, also referred to as *On-Off Keying* (OOK), obviously exhibits the best robustness against noise in ASK. A side benefit for increasing the modulation index to 100% is the power saving achieved by not spending energy to transmit logical 0's to the outside. Examples of using OOK only for data telemetry are (Yu & Bashirullah, 2006; Sodagar, et al, 2006 & 2009a).

Early attempts in designing IBM wireless links for both power and data telemetry employed ASK technique for modulation. The functional neuromuscular stimulator microsystem designed by (Akin & Najafi, 1994) is an example of a complete system that wirelessly receives power and data from the outside and returns backward data to the outside all using ASK modulation. Although ASK was successfully used for both power and data telemetry in several works (Von-Arx & Najafi, 1998; Yu & Najafi, 2001; Coulombe et al., 2003), it could not satisfy the somehow conflicting requirements for efficient telemetry of power and data at the same time. One of such conflicts can be explained as follows: The power regulator block needs to be designed to work desirably even when the amplitude received through the link is at A_L. For this purpose, A_L should be high enough to provide sufficient overhead voltage on top of the regulated voltage. On the other hand, it was explained before that A_H needs to be well above A_L in order to result in a high-quality data transfer, i.e., a low BER. This leads to two major problems:

- From the circuit design viewpoint, the regulator needs to be strong enough to suppress the large amplitude fluctuations associated with switchings between A_L and A_H. Not only these fluctuations are large in amplitude, they are also low in frequency as compared to the carrier frequency. This makes the design of the regulator challenging, especially if it is expected to be fully integrated.
- A_H values much higher than A_L are not welcomed from the standpoint of tissue safety either. This is because at A_H the amount of the power transferred through the tissue is much higher than what the system needs to receive (already guaranteed by the carrier energy at A_L).

Although ASK technique is a possible candidate for reverse data telemetry in the same way as the other modulation techniques are, it is a special choice in passive reverse telemetry. In this method, also known as *Load-Shift Keying* (LSK), reverse data is transferred back to the external host through the same link used for forward telemetry. While the forward data is modulated on the amplitude, frequency, or phase of the incoming carrier, backward data is modulated on the energy drawn through the link. The backward data is simply detected from the current flowing through the primary coil on the external side of the inductive link. What happens in the LSK method is, indeed, ASK modulation of the reverse data on the energy transferred through the link or on the current through the primary coil.

4.2.1 Frequency Shift Keying (FSK)

Three FSK demodulators are studied in (Ghovanloo & Najafi, 2004) that employ two carrier frequencies f_1 and $f_0=2f_1$ to transmit logic "1" and "0" levels, respectively. As a result, the minimum bit-time is $1/f_1$ and data rates higher than f_1 cannot be achieved. Moreover, by considering the average frequency as $(f_1+f_0)/2$, the DRCF ratio is limited to 67%. In all three circuits, FSK data is transmitted using a phase-coherent protocol, in which both of the carrier frequencies have a fixed phase at the start of each bit-time (Fig. 13). Whether a zero or 180° phase offset is chosen for sinusoidal FSK symbols, data bits are detected on the

receiver side by measuring the period of each received carrier cycle. In this case, every single long period (a single cycle of f_1) represents a "1" bit and every two successive short periods (two cycles of f_0) indicate a "0" bit. As illustrated in Fig. 14, in the demodulators reported by (Ghovanloo & Najafi, 2004), the received FSK carrier first passes through a clock regenerator block, which squares up the analog sinusoidal carrier. For period or, in general, time measurement in FSK demodulation, both analog and digital approaches have been examined.

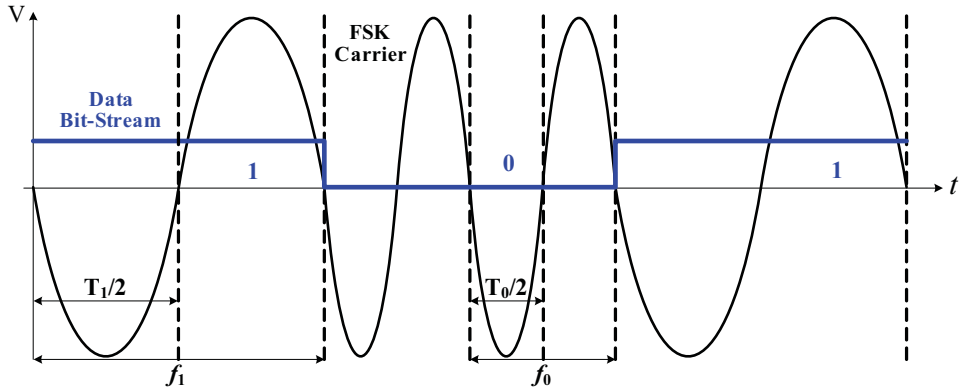

Fig. 13. Phase-coherent BFSK Modulation.

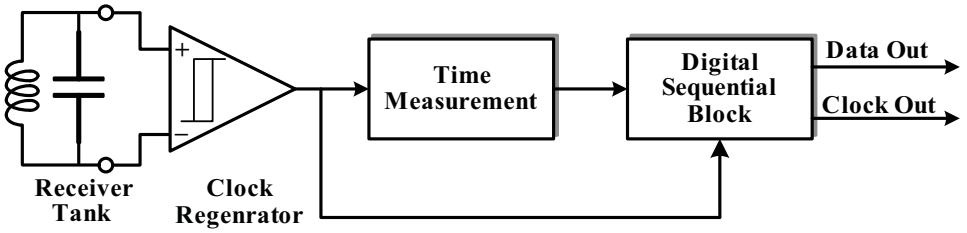

Fig. 14. General block diagram of the demodulators presented in (Ghovanloo & Najfi, 2004)

The analog approach is based on charging a capacitor with a constant current to examine if its voltage exceeds a certain threshold level (logic "1" detection) or not (logic "0" detection). In this method, charging and discharging the capacitor should be controlled by the logic levels of the digitized FSK carrier. The demodulator, in which the capacitor voltage is compared with a constant reference voltage, is known as *referenced differential FSK* (RDFSK) demodulator. On the other hand, in *fully differential FSK* (FDFSK) demodulator, two unequal capacitors are charged with different currents, and their voltages are compared by a Schmitt trigger comparator.

In the *digital FSK* (DFSK) demodulator scheme, duration of carrier cycles is measured with a 3-bit counter, which only runs at the first halves of the carrier cycles (i.e., during $T_1/2$ and $T_0/2$). The final count value of the counter is then compared with a constant reference number to determine whether a short or long period cycle has been received. The counter clock, which is provided by a 5-stage ring oscillator, is several times higher than f_0, and

should be chosen in such a way that the counter can discriminate between $T_1/2=1/(2f_1)$ and $T_0/2=1/(4f_1)$ time periods.
In all the three demodulators, the output of the comparator is fed into a digital block to generate the received data bit-stream. Additionally, detection of a long carrier cycle or two successive short carrier cycles in every bit-time is used along with the digitized FSK carrier to extract a constant frequency clock.
Measurement results of the three circuits in (Ghovanloo & Najafi, 2004) indicate that with 5 and 10 MHz carrier frequencies over a wideband inductive link, the DFSK demodulator has the highest data rate (2.5 Mbps) and the lowest power consumption. At lower carrier frequencies, however, since the current required to charge the capacitor in the RDFSK method can be very small, the RDFSK circuit might be more power efficient. On the other hand, due to the fact that the FDFSK demodulator benefits from a differential architecture, it is more robust against process variations. It should be noted that the inductive link used in (Ghovanloo & Najafi, 2004) was designed for both power and data transfer. Hence, data rate for the DFSK demodulator was limited to 2.5 Mbps in order to comply with the limited wireless link bandwidth set for efficient power transfer. In other words, the DFSK method would be capable of providing data rates as high as 5 Mbps (equal to the lower carrier frequency) if the link was designed merely for data telemetry.

4.2.3 Phase Shift Keying (PSK)

Recently, PSK modulation with constant amplitude symbols and fixed carrier frequency has attracted great attention in designing wireless links for IBMs (Zhou & Liu, 2007; Asgarian & Sodagar, 2009b; Simard et al., 2010). Demodulators based on both coherent and noncoherent schemes have been reported. In coherent detection, phase synchronization between the received signal and the receiver, called carrier recovery, is needed (Razavi, 1998). Therefore, noncoherent detectors are generally less complex and have wider usage in RF applications in spite of their higher BERs (Razavi, 1998). Coherent BPSK demodulators are mostly implemented by the COSTAS loop technique (Fig. 15), which is made up of two parallel *phase-locked-loops* (PLL). In Fig. 15, *d(t)* represents the transmitted data ("1" or "-1"), θ_1 is the received carrier phase, θ_2 is the phase of the oscillator output, and the upper and lower branches are called *in-phase* and *quadrature-phase* branches, respectively. In this method the goal is to control the local oscillator with a signal that is independent of the data stream (d(t)) and is only proportional to the *phase error* (θ_1-θ_2). In the locked state, phase error is approximately zero and the demodulated data is the output of the in-phase branch.
In order to reduce the complexity of conventional COSTAS-loop-based BPSK demodulators, nowadays, they are mainly designed by digital techniques such as filtering, phase shifting, and digital control oscillators (Sawan et al., 2005). Employing these techniques and inspiring from digital PLLs, a coherent BPSK demodulator is proposed in (Hu & Sawan, 2005). It is shown that the circuit behaves as a second-order linear PLL, and its natural frequency and damping factor are also calculated. Maximum data rate of the demodulator depends on the lock-in time of the loop which is determined by the natural frequency (Hu & Sawan, 2005). Increasing the natural frequency may decrease the damping factor and affect the dynamic performance of the system. Therefore, the maximum data rate measured for a 10-MHz carrier frequency is 1.12 Mbps, which results in a DRCF ratio of only 11.2% for this circuit. This idea is then evolved into a QPSK demodulator in (Deng et al., 2006) to achieve higher data rates. Moreover, improved version of the QPSK demodulator is studied in (Lu &

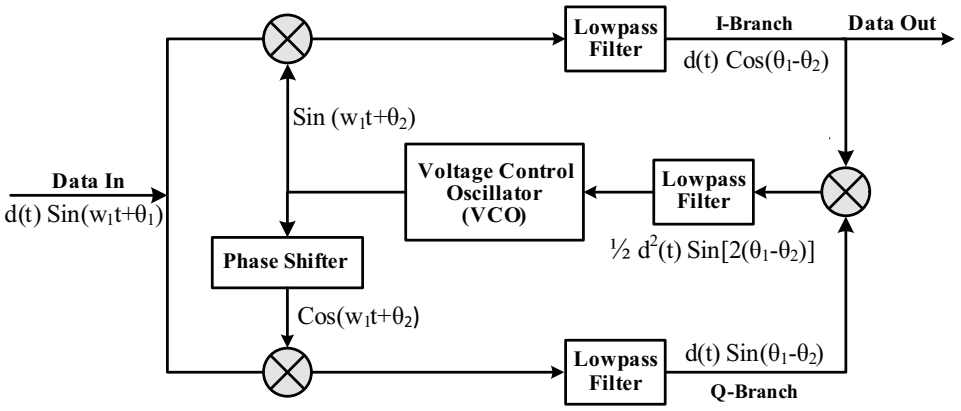

Fig. 15. COSTAS loop for BPSK demodulation.

Sawan, 2008) and is tested with a multiple carrier inductive link and a carrier frequency of 13.56 MHz in (Simard et al., 2010). According to the experimental results, maximum data rate and DRCF ratio for this circuit are 4.16 Mbps and about 30%, respectively.

Noncoherent BPSK demodulators can be implemented much simpler than coherent ones. Fig. 16 shows the general block diagram of two types of these demodulators presented in (Gong et al., 2008) and (Asgarian & Sodagar, 2009a). The received analog carrier first passes through a 1-bit *analog-to-digital converter* (ADC). Then, the *digitized carrier* (*BPSK*) is fed into the edge detection block, which contains two D flip-flops. By defining two sinusoidal waveforms with 180° phase difference associated with "0" and "1" symbols, this block can easily detect the received data based on either rising (logic "1") or falling (logic "0") edges of the digitized signal. Additionally, as both rising and falling edges occur in the middle of the symbol time ($T_{BPSK}/2$), detection of either edge can be used as a reference in the clock and data recovery unit in order to extract a clock signal from the received carrier and reconstruct the desired bit stream. Obviously, it is necessary to reset the D flip-flops after each detection, but it should also be noted that between any two (or more) consecutive similar symbols an edge occurs that should not be detected as a change in the received data. Hence, for proper operation of the demodulator, a reset signal is needed after each symbol time is over and before the edge of the next symbol (which takes place in the middle of it). For this purpose, in (Gong et al., 2008) a capacitor is connected to a Schmitt trigger comparator, whose output is the required reset signal. After each edge detection, this capacitor is charged towards the switching point of the comparator. Thus, its voltage rise time, which should have a value greater than $0.5T_{BPSK}$ and smaller than T_{BPSK}, is chosen to be $0.75T_{BPSK}$ in (Gong et al., 2008).

Another method of generating the reset signal is proposed by (Asgarian & Sodagar, 2009a), in which a 3-bit asynchronous counter has been designed in such a way that it starts counting after the detection of each edge. The *most significant bit* (MSB) of the counter goes high between $0.5T_{BPSK}$ and T_{BPSK}, and resets the D flip-flops. A free running 5-stage ring oscillator generates a *clock signal* (f_{osc}), which is used to prepare the clock of the counter. The oscillator frequency range is determined by the required activation time of the reset signal. As shown in Fig. 17, considering the two worst cases, the following conditions should be met

$$3T_{osc} > 0.5T_{BPSK}, \tag{14a}$$

and

$$4T_{osc} < T_{BPSK} . \quad (14b)$$

Therefore, frequency of the oscillator can be chosen between $4f_{BPSK}$ and $6f_{BPSK}$, which is set to $5f_{BPSK}$ in (Asgarian & Sodagar, 2009a).

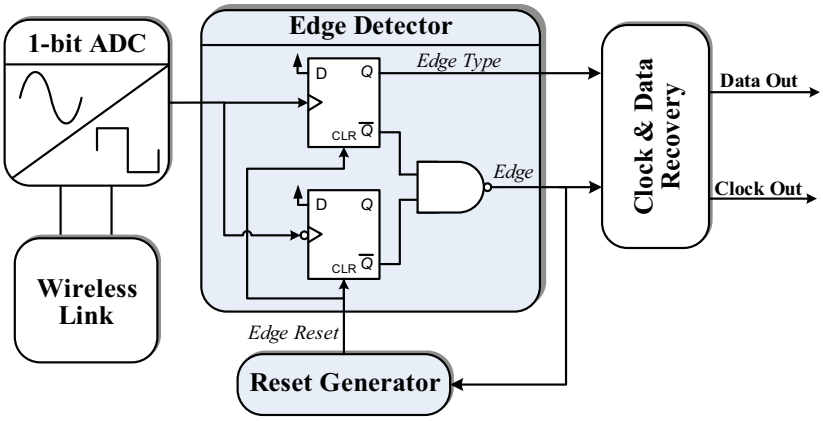

Fig. 16. General block diagram of two noncoherent demodulators presented in (Gong et al., 2008) and (Asgarian & Sodagar, 2009a).

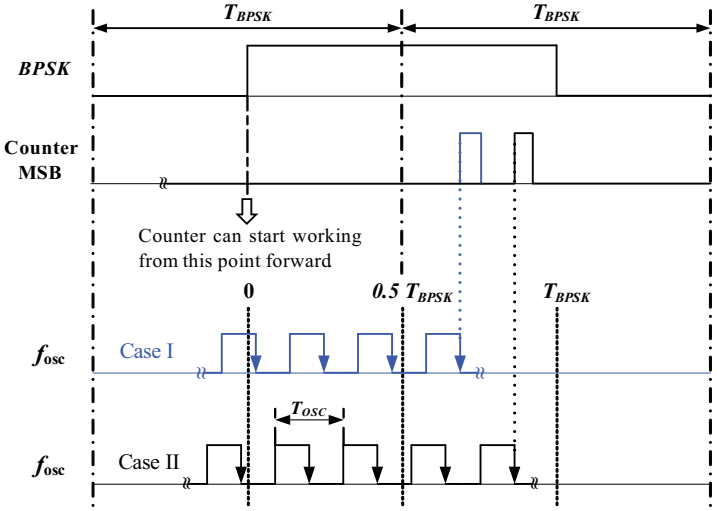

Fig. 17. Two worst cases for determining the range of f_{osc} in (Asgarian & Sodagar, 2009a)

Both of the described noncoherent BPSK demodulators have much lower power consumption than their coherent counterparts. Moreover, they can provide data rates equal to the carrier frequency provided that phase shifts are propagated through the wireless link quickly. In inductive links, this usually requires a low quality factor for the resonant circuits

on the primary and secondary sides of the link (Fig. 3), which leads to higher power dissipation. In (Wang et al., 2005) a PSK transmitter with *Q*-independent phase transition time is reported. The circuit, however, only modulates the phase of the carrier within two carrier cycles. Due to these limitations, experimental results of the demodulator studied in (Gong et al., 2008) with an inductive link, shows a DRCF ratio of only 20%. Similarly to the DFSK demodulator, this again emphasizes that in order to take advantage of the maximum demodulator speed, optimization of the data link in multiple carrier topologies is essential.

Most of the demodulators designed for IBMs can only operate with a specific carrier frequency, while their DRCF ratio is constant. In other words, at least one part of these circuits is dependent to the frequency of the modulated signal. For instance, in analog FSK demodulators (Ghovanloo & Najafi, 2004) and (Gong et al., 2008) the values of capacitors are determined based on the carrier frequency, or in (Hu & Sawan, 2005; Simard et al., 2010) the voltage controlled oscillator (VCO) is designed to work with a modulated carrier of 13.56 MHz. In (Asgarian & Sodagar, 2010) a *carrier-frequency-independent BPSK* (CFI-BPSK) demodulator is presented (Fig. 18). Similarly to (Asgarian & Sodagar, 2009a), the received data are detected based on rising or falling edge of the digitized carrier, while a new reset mechanism is proposed. As shown in Fig. 19, the required *reset signal* (*EdgeReset*) is generated by employing two *different digitized waveforms* (*BPSK*+ and *BPSK*-) of the received analog carrier. In this method, *EdgeReset* is activated after a falling edge occurs in both *BPSK*+ and *BPSK*- signals, and disabled with the first rising edge (or high level) of either *BPSK*+ or *BPSK*-. In order to fulfill these requirements, the reset generator is composed of a clipping circuit, and a control and edge detection block (Fig. 18). Experimental results of a prototype in (Asgarian & Sodagar, 2010) indicate that this circuit can achieve a DRCF ratio of 100% with capacitive links, while all of its components are independent of the carrier frequency.

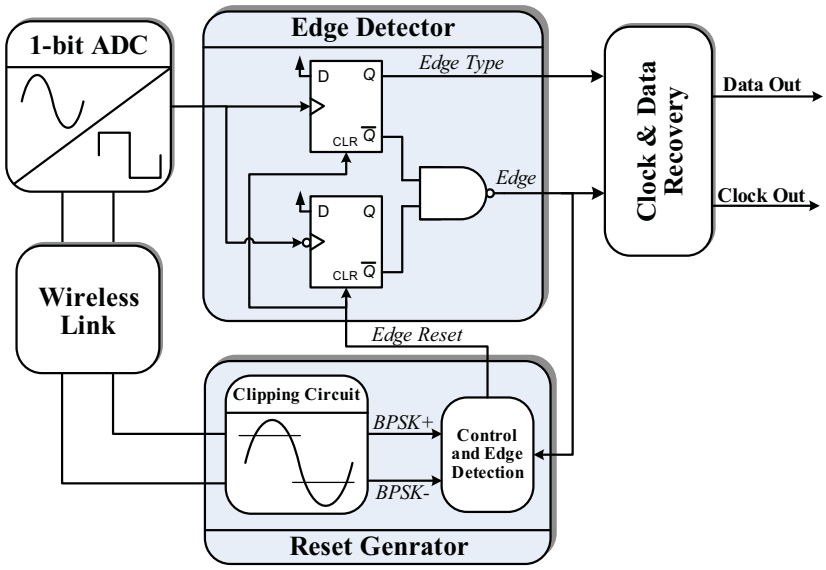

Fig. 18. Block diagram of the CFI-BPSK demodulator (Asgarian & Sodagar, 2010).

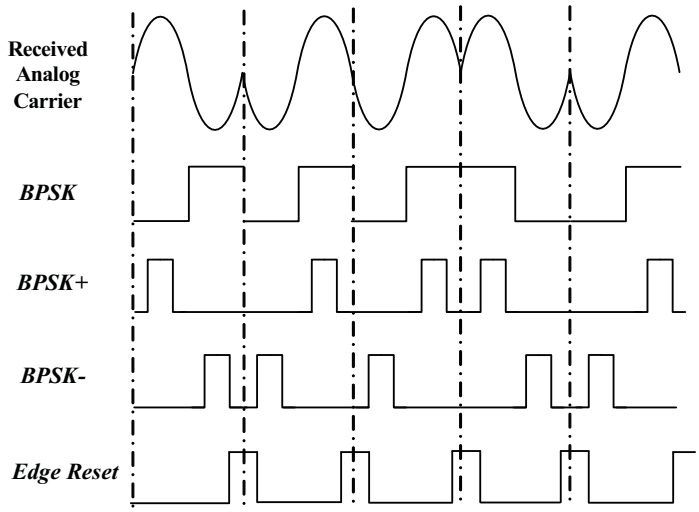

Fig. 19. Generating *EdgeReset* from the sinusoidal carrier in CFI-BPSK demodulator.

5. Conclusion

Wireless telemetry is one of the most important parts of IBMs, as it provides them with the power they require to operate, and also enables them to communicate with the external world wirelessly. Traditionally, wireless interfaces are implemented by inductive links. However, recently, employing capacitive links has been introduced as an alternative. Additionally, due to conflicting requirements of power and data telemetry, researches are mainly focused on utilizing multiple carrier or multiband links in both inductive and capacitive approaches. Besides size constraints, power dissipation in the human body is a key issue, especially in power telemetry where it may lead to excessive temperature increase in biological tissues. Hence, RF energy absorptions resulted from electromagnetic fields available in telemetry systems, should be evaluated by taking advantage of 3-D human body models and computational methods. In regards with forward data telemetry, recent works indicate that noncoherent BPSK demodulators are among the best choices for high data rate biomedical applications. These circuits are capable of providing DRCF ratios of up to 100%, provided that the link propagates phase shifts rapidly. This implies that the main speed limiting factor is going to be the wireless link and not the demodulator circuitry. Therefore, further optimization is needed in designing data links, where the capacitive method can potentially be a good solution.

6. References

Akin, T. & Najafi, K. (1998). A telemetrically powered and controlled implantable neural recording system with CMOS interface circuitry, *Proceedings of 7th Mediterranean Electrotechnical Conf.*, Vol. 2, pp. 545-548, Antalya, Apr. 1994.

Asgarian, F. & Sodagar, A.M. (2009a). A high-data-rate low-power BPSK demodulator and clock recovery circuit for implantable biomedical devices, *Proceedings of 4th Int. IEEE/EMBS Conf. Neural Eng.*, pp. 407-410, Antalya, Apr. 29–May 2, 2009.

Asgarian, F. & Sodagar, A.M. (2009b). A low-power noncoherent BPSK demodulator and clock recovery circuit for high-data-rate biomedical applications, *Proceedings of 31st Int. Conf. IEEE/EMBS*, pp. 4840-4843, Minnesota, Sep. 2009.

Asgarian, F. & Sodagar, A.M. (2010). A carrier frequency independent BPSK demodulator with 100% data-rate-to-carrier-frequency ratio, *Proceedings of IEEE Bio. Circuits and Systems Conf. (BioCAS)*, pp. 29-32, Paphos, Nov. 2010.

Baker, M.W. & Sarpeshkar, R. (2007). Feedback analysis and design of RF power links for low-power bionic systems, *IEEE Trans. Bio. Circuits and Systems*, Vol. 1, No. 1, Mar. 2007, pp. 28-38.

Canegallo, R.; Fazzi, A.; Ciccarelli, L.; Magagni, L.; Natali, F.; Rolandi, P.L.; Jung, E.; Di Cioccio, L. & Guerrieri, R. (2007). 3D capacitive interconnections for high speed interchip communication, *Proceedings of IEEE Custom Integrated Circuits Conf. (CICC)*, pp. 1-8, San Jose, Sept. 2007.

Christ, A.; Kainz, W.; Hahn, E.G.; Honegger, K.; Zefferer, M.; Neufeld, E.; Rascher, W.; Janka, R.; Bautz, W.; Chen, J.; Kiefer, B.; Schmitt, P.; Hollenbach, H.P.; Shen, J.; Oberle, M.; Szczerba, D.; Kam, A.; Guag, J.W. & Kuster, N. (2010). The Virtual Family—development of surface-based anatomical models of two adults and two children for dosimetric simulations, *Phys. Med. Biol.*, Vol. 55, No. 2, Jan. 2010, pp. 23-38.

Coulombe, J.; Gervais, J.-F. & Sawan, M. (2003). A cortical stimulator with monitoring capabilities using a novel 1 Mbps ASK data link, *Proceedings of IEEE Int. Symp. Circuits and Systems (ISCAS)*, Vol. 5, pp. 53-56, Bangkok, May 2003.

Culurciello, E. & Andreou, A. G. (2006). Capacitive inter-chip data and power transfer for 3-D VLSI, *IEEE Trans. Circuits and Systems-II*, Vol. 53, No. 12, Dec. 2006, pp. 1348-1352.

Deng, S.; Hu, Y. &. Sawan, M. (2006). A high data rate QPSK demodulator for inductively powered electronics implants, *Proceedings of IEEE Int. Symp. Circuits and Systems (ISCAS)*, pp. 2577-2580, Island of Kos, May 2006.

Dimbylow, P. (2005). Development of the female voxel phantom, NAOMI, and its application to calculations of induced current densities and electric fields from applied low frequency magnetic and electric fields, *Phys. Med. Biol.*, Vol. 50, No. 6, Mar. 2005, pp. 1047-1070.

Fazzi, A.; Canegallo, R.; Ciccarelli, L.; Magagani, L.; Natali, F.; Jung, E.; Rolandi, P. & Guerrieri, R. (2008). 3-D capacitive interconnections with monoand bi-directional capabilities, *IEEE J. Solid-State Circuits (JSSC)*, Vol. 43, No. 1, Jan. 2008, pp. 275-284.

Gabriel, C.; Gabriel, S. & Corthout, E. (1996a). The dielectric properties of biological tissues: I. Literature survey, *Phys. Med. Biol.*, Vol. 41, No. 11, Nov. 1996, pp. 2231-2249.

Gabriel, S.; Lau. R.W. & Gabriel, C. (1996b). The dielectric properties of biological tissues: II. Measurements in the frequency range 10 Hz to 20 GHz, *Phys. Med. Biol.*, Vol. 41, No. 11, Nov. 1996, pp. 2251-2269.

Gabriel, S.; Lau. R.W. & Gabriel, C. (1996c). The dielectric properties of biological tissues: III. Parametric models for the dielectric spectrum of tissues, *Phys. Med. Biol.*, Vol. 41, No. 11, Nov. 1996, pp. 2271-2293.

Ghovanloo, M & Najafi, K. (2004). A wideband frequency-shift keying wireless link for inductively powered biomedical implants, *IEEE Trans. Circuits and Systems-I*, Vol. 51, N0. 12, Dec. 2004, pp. 2374-2383.

Ghovanloo, M. & Alturi, S. (2007). A wide-band power-efficient inductive wireless link for implantable devices using multiple carriers, *IEEE Trans. Circuits and Systems-I*, Vol. 54, No. 10, Oct. 2007, pp. 2211-2221.

Gong, C.-S.A.; Shiue, M.-T.; Yao, K.-W. & Chen, T.-Y. (2008). Low-power and area-efficient PSK demodulator for wirelessly powered implantable command receivers, *Electronics Letters*, Vol. 44, No. 14, Jul. 2008, pp. 841-842.

Harrison, R.R. (2007). Designing efficient inductive power links for implantable devices, *Proceedings of IEEE Int. Symp. Circuits and Systems (ISCAS)*, pp. 2080-2083, New Orleans, May 2007.

Hu, Y. & Sawan, M. (2005). A fully-integrated low-power BPSK demodulator for implantable medical devices, *IEEE Trans. Circuits and Systems-I*, Vol. 52, No. 12, pp. 2552-2562, Dec. 2005.

IEEE Standard C95.1-2005. *IEEE standards for safety levels with respect to human exposure to radio frequency electromagnetic fields, 3 KHz to 300 GHz*.

Jow, U.-M. & Ghovanloo, M. (2007). Design and optimization of printed spiral coils for efficient transcutaneous inductive power transmission, *IEEE Trans. Bio. Circuits and Systems*, Vol. 1, No. 3, Sep. 2007, pp. 193-202.

Jow, U.-M. & Ghovanloo, M. (2008). Optimization of a multiband wireless link for neuroprosthetic implantable devices, *Proceedings of IEEE Bio. Circuits and Systems Conf. (BioCAS)*, pp. 97-100, Baltimore, Nov. 2008.

Jow, U.-M. & Ghovanloo, M. (2009). Modeling and optimization of printed spiral coils in air, saline, and muscle tissue environments, *IEEE Trans. Bio. Circuits and Systems*, Vol. 3, No. 5, Oct. 2009, pp. 339-347.

Kendir, G.A.; Liu, W.; Wang, G.; Sivaprakasam, M.; Bashirullah, R.; Humayun, M.S. & Weiland, J.D. (2005). An optimal design methodology for inductive power link with class-E amplifier, *IEEE Trans. Circuits and Systems-I*, Vol. 52, No. 5, pp. 857-866, May 2005.

Lazzi, G. (2005). Thermal effects of implants, *IEEE Eng. Med. Bio. Mag.*, Vol. 24, No. 5, Oct. 2005, pp. 75-81.

Lin, J.C. (1986). Computer methods for field intensity predictions, In: *CRC Handbook of Biological Effects of Electromagnetic Fields*, C. Polk and E. Postow, Eds., Ch. 2, pp. 273-313, CRC, Boca Raton, FL.

Liu, W.; Sivaprakasam, M.; Wang, G.; Zhou. M.; Granacki, J.; Lacoss, J. & Wills, J. (2005). Implantable biomimetic microelectronic systems design, *IEEE Eng. Med. Bio. Mag.*, Vol. 24, No. 5, Oct. 2005, pp. 66-74.

Lu, Z. & Sawan, M. (2008). An 8 Mbps data rate transmission by inductive link dedicated to implantable devices, *Proceedings of IEEE Int. Symp. Circuits and Systems (ISCAS)*, pp. 3057-3060, Seattle, May 2008.

Razavi, B. (1998). *RF Microelectronics*, Prentice-Hall Inc., 0-13-887571-5, USA.

Sawan, M.; Hu, Y. & Coulombe, J. (2005). Wireless smart implants dedicated to multichannel monitoring and microstimulation, *IEEE Circuits and Systems Mag*., Vol. 5, No. 1, 2005, pp. 21-39.

Shah, M.R.; Phillips, R.P. & Normann, R.A. (1998). A study of printed spiral coils for neuroprosthetic transcranial telemetry applications, *IEEE Trans. Bio. Eng*., Vol. 45, No. 7, Jul. 1998, pp. 867-876.

Simard, G.; Sawan, M. & Massicotte, D. (2010). High-Speed OQPSK and efficient power transfer through inductive link for biomedical implants, *IEEE Trans. Bio. Circuits and Systems*, Vol. 4, No. 3, Jun. 2010, pp. 192-200.

Singh, V.; Qusba, A.; Roy, A.; Castro, R.A.; McClure, K.; Dai, D.; Greenberg, R.J.; Weiland, J.D.; Humayun, M.S. & Lazzi, G. (2009). Specific absorption rate and current densities in the human eye and head induced by the telemetry link of an epiretinal prosthesis, *IEEE Trans. Antennas and Propagation*, Vol. 57, No. 10, part 2, Oct. 2009, pp. 3110-3118.

Sodagar, A.M. & Najafi, K. (2006). Wireless interfaces for implantable biomedical microsystems, *Proceedings of IEEE Int. Midwest Symp. Circuits and Systems (MWSCAS)*, Vol. 2, pp. 265-269, Aug. 2006.

Sodagar, A.M.; Wise, K.D. & Najafi, K. (2006). An interface chip for power and bidirectional data telemetry in an implantable cochlear microsystem, *Proceedings of IEEE Bio. Circuits and Systems Conf. (BioCAS)*, pp. 1-4, London, Nov. 29 2006-Dec. 1 2006.

Sodagar, A.M. & Amiri, P. (2009). Capacitive coupling for power and data telemetry to implantable biomedical microsystems, *Proceedings of 4th Int. IEEE/EMBS Conf. Neural Eng*., pp. 411-414, Antalya, April 29–May 2, 2009.

Sodagar, A.M.; Perlin, G.E.; Yao, Y.; Najafi, K. & Wise, K.D. (2009a). An implantable 64-channel wireless microsystem for single-unit neural recording, *IEEE J. Solid-State Circuits (JSSC)*, Vol. 44, No. 9, Sep. 2009, pp. 2951-2604.

Sodagar, A.M.; Wise, K.D. & Najafi, K. (2009b). A wireless implantable microsystem for multichannel neural recording, IEEE *Trans. Microwave Theory and Techniques*, Vol. 57, No. 10, Oct. 2009, pp. 2565-2573.

Sokal, N.O. & Sokal, A.D. (1975). Class E-A new class of high-efficiency tuned single-ended switching power amplifiers, *IEEE J. Solid-State Circuits (JSSC)*, Vol. 10, No. 3, Jun. 1975, pp. 168-175.

Van Schuglenbergh, K. & Puers, R. (2009). *Inductive Powering, Basic Theory and Application to Biomedical Systems,* Springer, 978-90-481-2411-4.

Von-Arx, J.A. & Najafi, K. (1999). A wireless single-chip telemetry-powered neural stimulation system, *Technical Digest, IEEE Int. Solid-State Circuits Conf. (ISSCC)*, pp. 214-215, San Francisco, Feb. 1999.

Wang, G.; Liu, W.; Sivaprakasam, M.; Zhou, M.; Weiland, J.D. & Humayun, M.S. (2005). A wireless phase shift keying transmitter with Q-independent phase transition time, *Proceedings of 27th Int. Conf. IEEE/EMBS*, pp. 5238-5241, Shanghai, Sep. 2005.

Yu, H. & Najafi, K. (2001). Circuitry for a wireless microsystem for neural recording microprobes, *Proceedings of 23rd Int. Conf. IEEE/EMBS*, Vol. 1, pp. 761-764, Istanbul, Oct. 2001.

Yu, H. & Bashirullah, R. (2006). A low power ASK clock and data recovery circuit for wireless implantable electronics, *Proceedings of IEEE Custom Integrated Circuits Conf. (CICC)*, pp. 249-252, San Jose, Sept. 2006.

Zhou, M. & Liu, M. (2007). A non-coherent PSK receiver with interference-canceling for transcutaneous neural implants, *Technical Digest, IEEE Int. Solid-State Circuits Conf. (ISSCC)*, pp. 156-593, San Francisco, Feb. 1997.